Bulletin of Geophysics and Oceanography Vol. XX, n. X, pp. XXX-XXX; Xxxxx 20xx
DOI 10.4430/bgo00456

Library and field-referenced spectra applied in enhancing extraction effects of remotely-sensed hydrothermal alteration minerals: a case study at the Muteh gold mining district in Iran

K. Mokhtari[1], H. Asadi Haroni[1,2], M.A. Aliabadi[1] and S. Beyranvand[1]

[1] *Department of Geology, Mahallat Branch, Islamic Azad University, Mahallat, Iran*
[2] *Department of Mining Engineering, Isfahan University of Technology, Isfahan, Iran*

(Received: 31 May 2023; accepted: 4 March 2024; published online: 13 June 2024)

ABSTRACT The orogenic gold mineralisation at the Muteh mining district in Iran is hosted by silica-iron oxide veins associated with phyllic (sericite), argillic (kaolinite), and propylitic (chlorite) hydrothermal alterations. Advanced Spaceborne Thermal Emission and Reflection Radiometer (ASTER) data of the district were initially processed by using library spectra and standard image processing techniques to map minerals associated with gold mineralisation. Image processing techniques were also applied to the Sentinel-2A and Landsat-8 satellite data to map lineaments and alterations. Then, the spectral behaviour of 24-field alteration samples, mostly associated with gold mineralisation, was obtained from a handheld spectrometer and applied to the ASTER data using the spectral angle mapper (SAM) and matched filtering methods for mapping favourable alteration and iron oxide minerals. The identified minerals were compared with the known gold deposits and validated by further field sampling and chemical analyses. The results showed that favourable alteration minerals, identified by the ASTER data using field-referenced spectra, are better correlated with the zones of gold mineralisation, compared to those identified by using library spectra. Processing ASTER data by using field-reference spectra and the SAM method is recommended for mapping favourable alteration minerals in similar geologic settings for organic gold exploration elsewhere.

Key words: remote sensing, spectral analysis, alteration mapping, gold, target selection.

1. Introduction

Mineralogical and chemical changes in rocks, caused by hydrothermal alteration processes, often affect the amount of reflected and/or absorbed energy, which could be measured by spectral analyses of field samples and processing satellite imagery data to identify minerals indicative of the hydrothermal alterations, associated with certain mineral deposits. In recent years, based on the spectral behaviour of minerals, by using library spectra or field spectrometers, remote sensing has played an important role, in the field of mineral exploration, in mapping hydrothermal alterations and rock units associated with various types of mineralisation (Sadek, 2005; Sadek *et al*., 2006; Gad and Kusky, 2007; Arghavanian *et al*., 2011; Yazdi *et al*., 2011; Hassan *et al*., 2014; Akbari *et al*., 2015; Gabr *et al*., 2015; Hassan and Ramadan, 2015; Ali-Bik *et al*., 2017, 2018; Asran and Hassan, 2019; Shokry *et al*., 2021; Ghoneim *et al*., 2022). The spectral behaviour of minerals is identified by means of portable short-wave infrared (SWIR) field spectrometers,

such as the TerraSpec spectrometer and the Portable Infrared Mineral Analyser (PIMA), and can be widely used in mineral exploration to process satellite imagery data (van Ruitenbeek *et al*., 2005; Dukart *et al*., 2006; Chang and Yang, 2012; Huang *et al*., 2018). These instruments are useful for identifying clays and other hydrous minerals such as epidote, chlorite, micas (illite, muscovite, and phengite), calcite, dickite, and gypsum. Compared to standard mineralogical studies and geochemical analyses, these techniques present many advantages such as fast and nondestructive measurements, no sample preparation, and relatively low costs (Chang and Yang, 2012).

Advanced Spaceborne Thermal Emission and Reflection Radiometer (ASTER), Sentinel-2A, and Landsat-8 satellite imagery data have been used in this research to map hydrothermal alteration minerals, iron oxides, and lineaments of the Muteh gold mining district, located in central Iran and covering an area of approximately 400 km^2. The ASTER sensor is a multispectral instrument that measures visible, near-infrared, and shortwave infrared portions of the electromagnetic spectrum. These spectrum portions can be used by various image-processing techniques such as the spectral angle mapper (SAM) and matched filtering (MF) methods utilised to map hydrothermal alterations, structures, iron oxides, and certain lithological units (Moore *et al*., 2008; Irons *et al*., 2012; Rasouli and Tangestani, 2020; Zerai *et al*., 2023). The Sentinel-2A satellite, with a 10-metre spatial resolution and a 16-bit radiometric resolution, is the latest generation of observation missions from the European Space Agency (ESA). Sentinel-2A satellite data are used in this research to locate structural features and improve the spatial resolution of the ASTER data. Landsat-8 satellite imagery data is used to determine and compare hydroxyl-bearing clay alterations and iron oxides with the results of the processed ASTER data. Landsat-8 satellite data includes a band in the absorption range (band 2) and a band in the high reflection range (band 4) in the visible near-infrared (VNIR) portion of the electromagnetic spectrum, which may be used to identify iron oxides including goethite, hematite, and jarosite (Yuhas *et al*., 1992). Compared to Landsat-8 satellite data, Sentinel-2A data has a higher spectral, spatial, and temporal resolution (Immitzer *et al*., 2016; Lefebvre *et al*., 2016; Paul *et al*., 2016; Pesaresi *et al*., 2016).

Previous remote sensing researches at the Muteh gold mining district were mostly focused on processing Landsat and ASTER satellite imagery data just by using United State Geological Survey (USGS) library spectra and standard image processing methods (Asadi Haroni and Tabatabei, 2016; Mokhtari *et al*., 2023). The main objective of this research is to use spectral measurements of field samples in processing the ASTER satellite imagery data for mapping hydrothermal alteration minerals and iron oxides possibly associated with the orogenic gold mineralisation. The results are compared with the hydrothermal alteration minerals and iron oxides identified by using the USGS library spectra and are validated by field information so as to propose the optimal image processing approach for the regional exploration of orogenic gold mineralisation.

2. Geology and mineralisation of the Muteh area

The Muteh gold mining district includes several gold deposits/occurrences such as Chah Khatoon, Senjedeh, Darre Ashki, Tangehzar, Cheshmeh Gohar, Ghorom Ghorom, Cheshmeh Dastar, Chah Allameh, and Sekolop (Fig. 1a). The main mineralisation in this district is organic gold type in character, and the ore is currently mined at the Senjedeh and Chah Khatoon deposits (Moritz *et al*., 2006). This district is located in the central part of the Sanandaj-Sirjan zone (SSZ)

(Fig. 1b), mostly covered by metamorphic rocks (amphibolite, gneiss, greens schist, greywacke, phyllite, and quartzite), igneous complexes (rhyolite, dacite, granite-granodiorite, and andesite) and sedimentary rocks of limestone, dolomite, shale, travertine, conglomerate, and marl (Figs. 1, 2, and 3) (Farhangi, 1982; Tavakoli Dehkordi, 1986; Yusefinia, 2004).

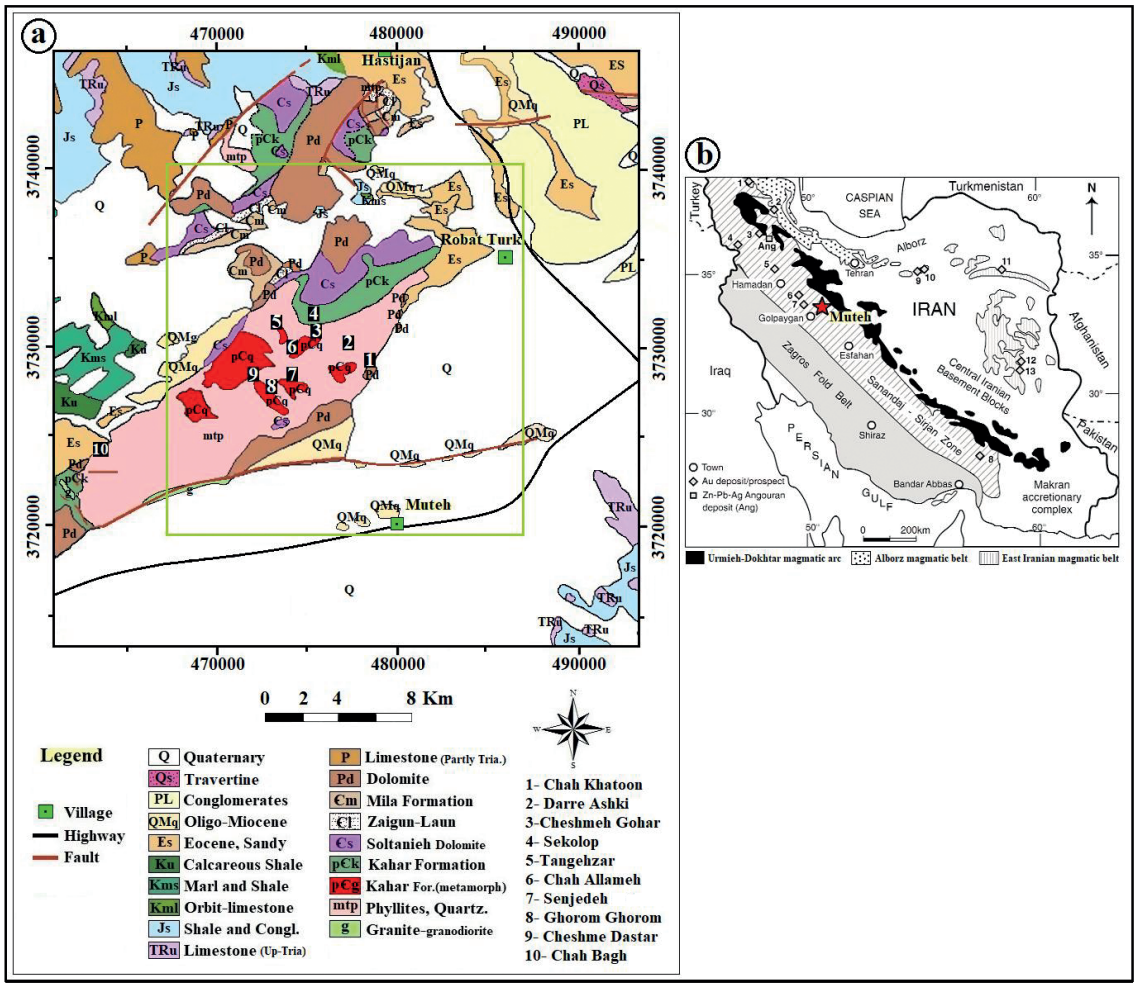

Fig. 1 - a) Geological map of the Muteh gold mining district with the location of gold deposits/occurrences (simplified from the 1:250,000 geological map of Golpayegan), and b) tectono-magmatic map of Iran showing the location of the Muteh district in the Sanandaj-Sirjan zone (modified after Moritz *et al*., 2006).

The orogenic gold mineralisation at the Muteh district is mainly associated with silica, phyllic, and argillic hydrothermal alterations, and iron oxides, mostly concentrated in the form of quartz veins in the fractures of highly altered meta rhyolite host rocks (Moritz *et al*., 2006) (Fig. 3). The mineralised zones mostly contain large amounts of sulphide minerals (locally up to 20%) including euhedral to subhedral pyrite, chalcopyrite, and arsenopyrite in the host rocks of leached meta rhyolite and various types of metamorphosed shales. In addition, they also contain large amounts of quartz-sulphide veins formed along a ductile-brittle shear zone. Pyrite and chalcopyrite are the major minerals associated with the gold mineralisation. Marcasite,

bismuthite, arsenopyrite, and pyrite are other minerals present in the gold mineralised zones (Mehrabi *et al*., 2012) (Fig. 3).

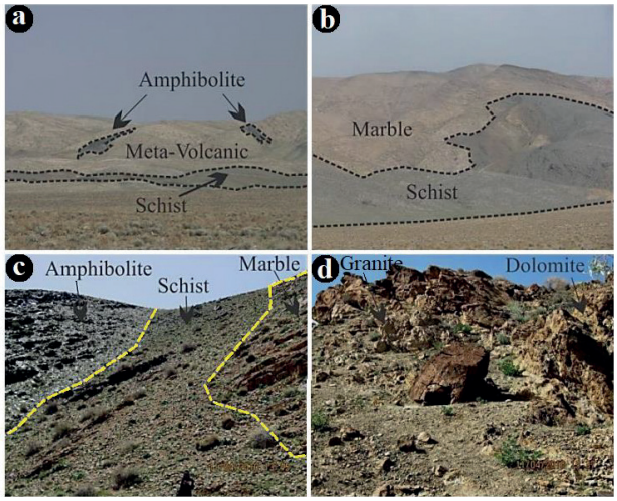

Fig. 2 - Field views of outcrops in the Muteh gold mining district: a) amphibolite, meta-volcanic, and schist; b) Palaeozoic marble under Jurassic schist; c) the succession of the amphibolite, schist, and marble layers; d) granite intrusion into Permian dolomite (Karimi *et al.*, 2012).

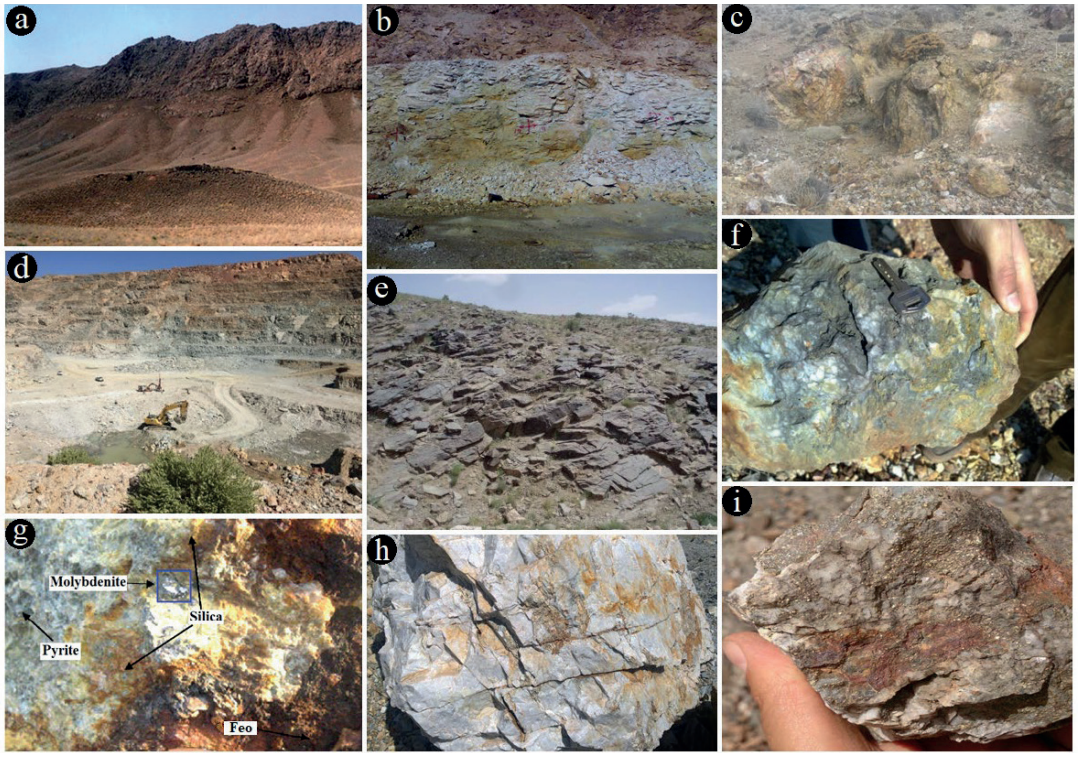

Fig. 3 - Field views of outcrops and hand specimens from the hydrothermal alterations and iron oxides in the Muteh district: a) metamorphic rocks, limestone, and dolomite with iron oxide lenses; b) silicic-argillic alteration at the Senjedeh gold deposit; c) silicification and argillic alteration at the Senjedeh deposit; d) mining activities at the Chah Khatoon gold deposit showing phyllic-argillic alteration; e) meta rhyolite units showing pyrite decomposition into iron oxides; f) sulphide ore containing pyrite and arsenopyrite at the Senjedeh deposit; g) molybdenite in the pyrite-bearing quartz-sericite alteration zone; h) strong silicification; i) pyrites, partly oxidised to hematite and goethite.

3. Methods

3.1. Remote sensing

A cloud-free L1T-ASTER scene (60×60 km^2) in the Muteh area, acquired on 13 September 2003, was downloaded from the USGS website. It was orthorectified and reprojected to UTM zone 39N/WGS-84 by the Geosense company in the Netherlands, using the SRTM (Shuttle Radar Topography Mission) Digital Elevation Model and orthorectified Landsat ETM+ Satellite data of the area as reference materials. The Landsat-8 data of the area (path 164 and line 37) was acquired on 2 June 2017 and downloaded from the USGS website. The Sentinel-2A satellite scene, acquired on 14 September 2020, corresponds to the L1C information level and was downloaded from the ESA website. Atmospheric correction was applied to the ASTER data by using the FLASH algorithm to obtain the proper image of the Earth's surface reflectance for spectral analyses. The Sentinel-2A satellite data was obtained in the L1C correction plane, so the 3D radiometric and geometric corrections were made through reflectance correction.

3.2. Field survey and laboratory investigation

To perform the spectral analysis of the ASTER data, in total 24 samples were collected from various hydrothermal alteration zones of the Senjedeh and Chah Khatoon gold deposit areas, located in the central parts of the Muteh gold mining district, and 83 measurements were obtained from these samples by using a TerraSpec spectrometer at the Geosense company in the Netherlands. Some of these samples were also analysed by X-ray diffraction (XRD), induced coupled plasma mass spectroscopy (ICP-MS), and atomic absorption spectrometry (AAS) to validate hydrothermal alteration minerals and associated gold mineralisation mapped by the ASTER data.

3.3. TerraSpec spectrometer

Various spectrometers, such as portable infrared mineral analysers and analytical spectroscopy devices, can be used to record the spectral properties of various materials (Hosseinjani Zadeh, 2013). The TerraSpec spectrometer, which was used in this research, is a portable mineral identification device that is typically equipped with hundreds of low-bandwidth spectral channels to measure the spectral properties of materials in the laboratory or field over a wide range of wavelengths (350-2,500 nm). The measured reflectance values at each wavelength are the result of spectroscopy, which is recorded as a spectral reflectance diagram.

4. Image processing and interpretation of satellite data

Satellite data can be processed by using visual and digital methods. By combining these two methods, mineral exploration targets can be identified more reliably. Colour composite, band ratio, principal component analysis (PCA), and spectral analyses (e.g. SAM and MF) are examples of image processing methods used in this research.

To increase the spatial resolution of the ASTER images, the Sentinel-2A data of the study area, with a 10-metre spatial resolution and 16-bit radiometric resolution, were used by the data fusion method to improve the spatial detection capability and interpretation of the alteration

zones. Data fusion was performed by resampling the ASTER data with higher-resolution Sentinel-2A data using the nearest neighbour method. The location of the 24 samples, collected for the spectral measurements, is shown in a high-resolution ASTER image, resampled by a Sentinel-2A image of the central part of the Muteh district (Fig. 4).

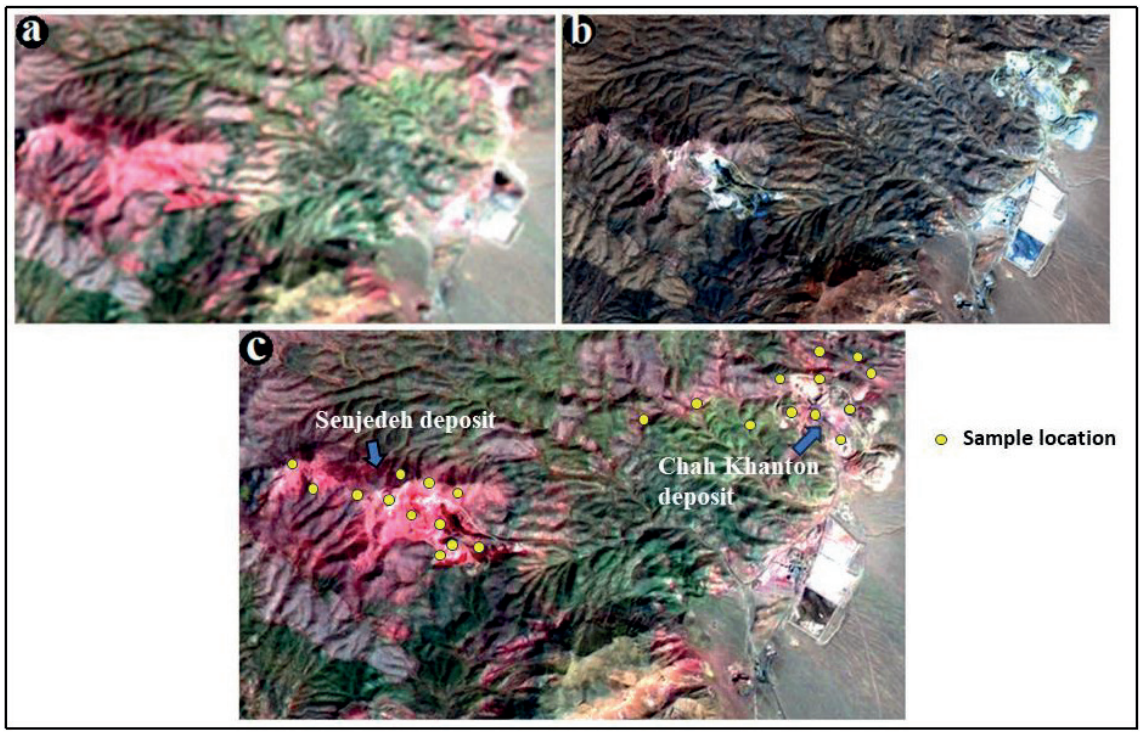

Fig. 4 - a) Band combination RGB468 ASTER data with a 30-metre pixel size showing the hydrothermal clay alterations in pink pixels; b) Sentinel-2A natural colour composite with a 10-metre pixel size showing the hydrothermal clay alterations in white pixels; c) the resampled RGB468 ASTER image with the 10-metre pixel size Sentinel-2A image showing the hydrothermal clay alterations, in pink-white pixels, with an improved resolution, compared to the ASTER image; the yellow circles are field sample locations collected from the two active mining areas of the Senjedeh and Chah Khatoon deposits (in the central part of the Muteh district) for spectral measurements.

4.1. Colour composite images

Colour composite images, using different bands and their visual interpretation, are a common approach for identifying hydrothermal alteration zones and associated minerals (Vincent, 1997). A colour composite image is created by combining three different bands to each of which the three primary colours (RGB) are assigned. Other types of band combinations displayed in terms of RGB are called false colour composites (Vincent, 1997). The images from the ASTER sensor lack the blue band, and the colour combination resulting from the visible near-infrared (VNIR) bands is a false-colour composite image showing vegetation in red pixels (Fig. 5a). By using images created by other image processing techniques, such as PCA and band ratio, and placing proper spectral bands in the correct RGB channels, various colour composite images can be generated for interpretation (Gupta, 1991; Ahmadi *et al.*, 2022).

Fig. 5b shows the Landsat-8 colour composite image (RGB642) of the Muteh district. In this

colour composite, hydroxyl-bearing clay minerals are shown in bright pixels. Some of the colour composites of the ASTER data that are often used to visually identify zones of hydrothermal alterations are shown in Table 1 (Karimpoor, 2005).

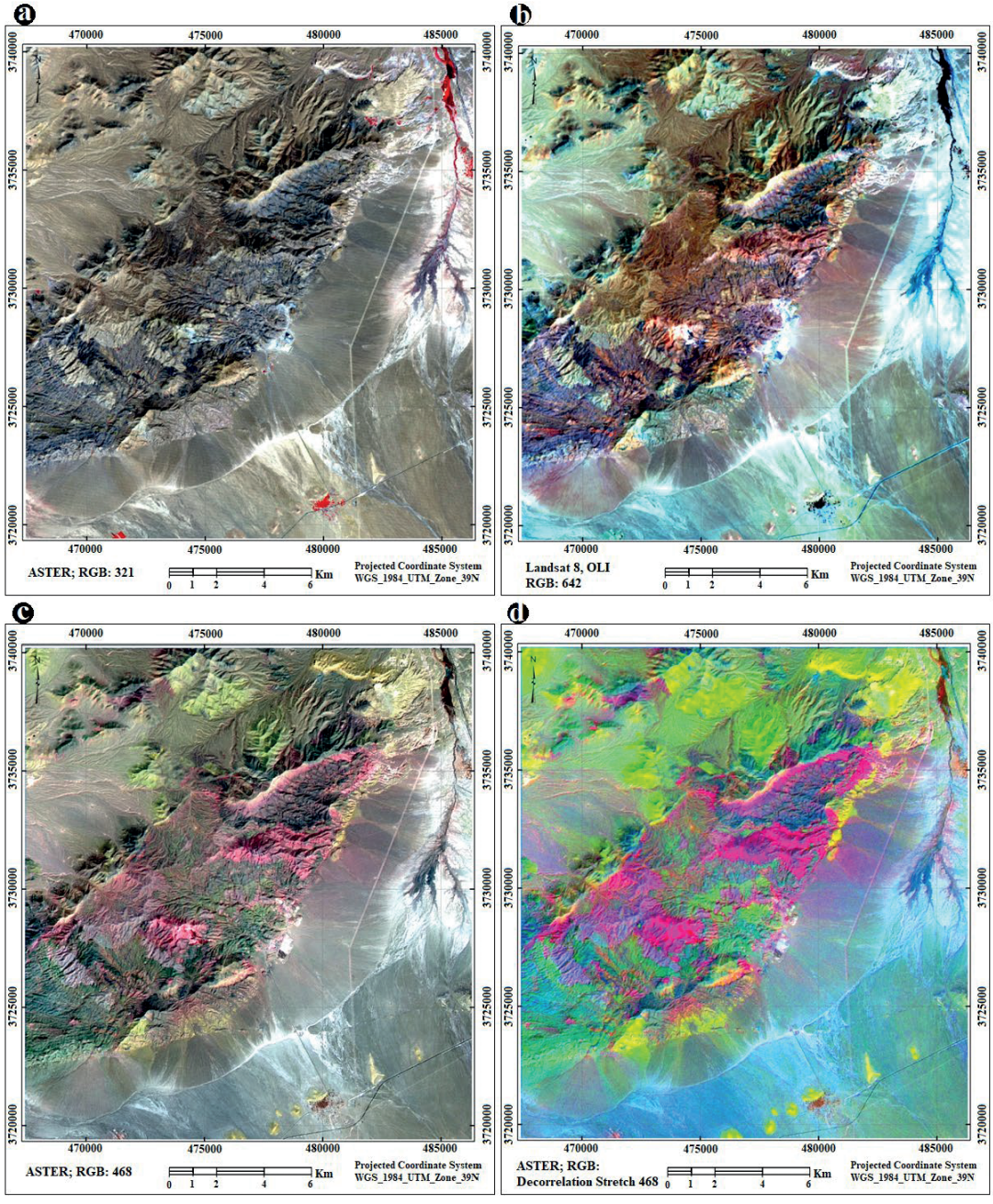

Fig. 5 - a) The standard colour combination (RGB321) of the ASTER data in the visible near-infrared (VNIR) region, showing the vegetation in red pixels; b) the Landsat-8 colour combination image of the RGB642, showing the hydrothermal alteration in white pixels; c) the colour combination image of the ASTER data (RGB468) in the shortwave infrared (SWIR) region, showing the hydrothermal alteration in pink pixels, and d) the decorrelation stretch image of the RGB468, showing the hydrothermal alterations in red pixels (modified after Mokhtari *et al*., 2023).

Table 1 - Some general colour combinations in ASTER data for mapping various hydrothermal alteration minerals (Karimpoor, 2005).

RGB display of ASTER bands	Red	Green	Blue	Pink	Orange
SWIR 456	kaolinite			alunite -kaolinite	sericite
SWIR 468	alunite	epidote-chlorite	chlorite	kaolinite	sericite
TIR 531	silica			silicate rocks	

Experimental evaluations have shown that the RGB468 image of the ASTER data is one of the most appropriate images to visually locate zones of hydrothermal alteration in many types of mineral systems such as porphyry copper and epithermal gold deposits (Ferrier *et al*., 2002). The ASTER data are also effectively used to distinguish carbonate minerals such as calcite and dolomite (Rasouli and Tangestani, 2020). The RGB468 image of the study area shows the phyllic and argillic alteration zones in colours ranging from pink to red and the propylitic alterations in dark green (Fig. 5c). The pink-to-red pixels, associated with phyllic to argillic alteration, are due to the high reflectance feature across band 4 in the SWIR region.

Satellite bands with high correlation usually result in soft colour combinations. By removing the high correlation that is usually present in multispectral images, more effective colour combination images can be created. Using the decorrelation stretching algorithm, to remove the high correlations from combination bands, produces colour composite images that are very useful for changing the detection zone. The decorrelation stretch of the RGB468 image of the ASTER data in the study area shows the phyllic and argillic alteration zones in pink, propylitic alteration in dark green, and carbonate formations in a range from yellow to a more pronounced green (Fig. 5d).

The ASTER sensor is also equipped with five thermal infrared (TIR) bands with a 90-metre spatial resolution and 12-bit radiometric resolution so that the application of these bands enables detecting and distinguishing silicification zones. In the colour composite image obtained with bands 14, 12, and 10, hydrothermal silicification zones, possibly associated with gold mineralisation, are shown in colours ranging from red to dark brown pixels, while the carbonate rocks are shown in dark pixels (Fig. 6). The red-to-dark brown pixels associated with silicification are due to the high thermal emission across band 14 in the TIR region.

4.2. Band ratio

Band ratio is a digital approach in multispectral image processing in which the pixels in one image are divided by the corresponding pixels of another image. By using proper band ratios based on the understanding of the spectral characteristics of minerals, various features, such as hydrothermal alterations and rock units, can be identified (Di Tommaso and Rubinstein, 2007). Band ratio is commonly used in mineralogical and petrological mapping as it highlights the spectral features of the target material from the surrounding environment while reducing the effects of slope variations and changes in topographic directions (Mahanta and Maiti, 2021). Due to the fact that hydroxyl minerals show high reflectance features in band 6 of the Landsat-8 satellite data and high absorption features in band 7, a band ratio of 6/7 was created to enhance these minerals (Fig. 7a).

Fig. 7b shows the colour composite image of the band ratios (R: 6/7, G: 6/5, and B: 4/2) of the Landsat-8 data of the study area. In this band ratio combination, the orange pixels represent

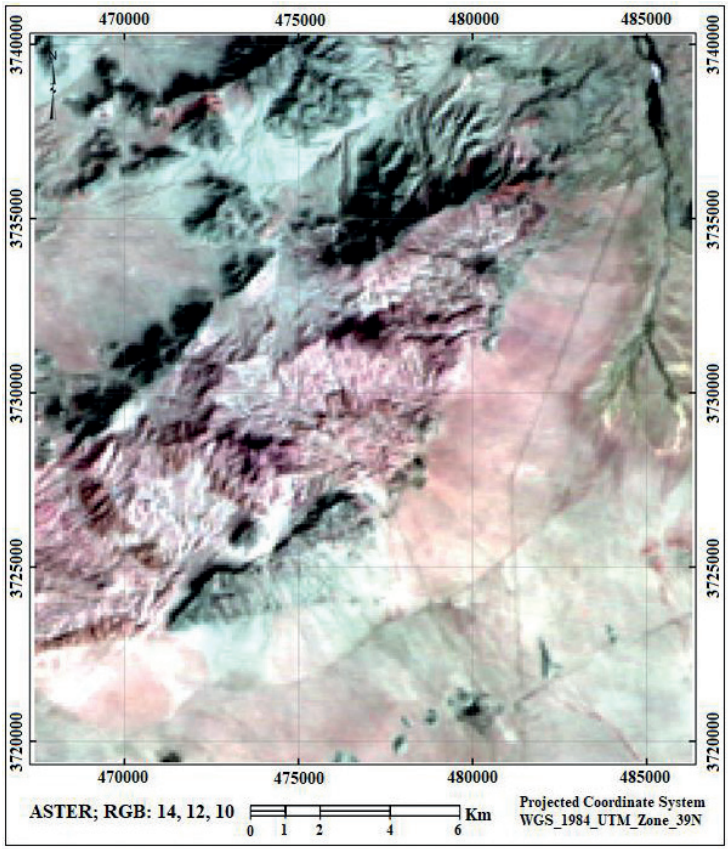

Fig. 6 - Colour composite image of the thermal ASTER data (TIR14, 12, and 10) in the Muteh district, showing silicification zones in red-to-dark brown pixels and carbonate rocks in dark pixels.

phyllic alteration (e.g. sericite), the pink pixels represent argillic alteration (e.g. kaolinite), the green pixels represent propylitic alteration (e.g. chlorite), the blue pixels represent carbonates (e.g. calcite), and the yellow pixels represent vegetation. In the ASTER data, silica shows a high reflectance feature in band 14 and a high absorption feature in band 12, and, therefore, the 14/12 band ratio image in the TIR region is an effective approach to detect silicification (bright pixels in Fig. 7c).

4.3. Principal component analysis (PCA)

PCA is generally used for data compression, while in remote sensing it is used to remove spectral redundancy data and concentrate relatively correlated multiple band data into one band with high variance (Alavipanah, 2003). The feature-oriented principal component selection (FPCS) approach, or the well-known Crosta technique, uses favourable input bands to identify favourable features in the output components (Crosta and Moore, 1989). This approach is well suited to distinguish zones of hydrothermal alteration and iron oxides in metallogenic provinces (Abrams *et al*., 1983; Crosta and Moore, 1989; Loughlin, 1991; Bennett *et al*., 1993; Ruiz-Armenta and Prol-Ledesma, 1998; Tangestani and Moore, 2002).

The FPCS approach was applied to Landsat-8 imagery data of the study area to identify iron oxides and zones of hydrothermal alteration related to general hydroxyl-bearing minerals. Considering the spectral reflectance diagram of various hydroxyl-bearing minerals, which are the main components of hydrothermal alterations, bands 2, 5, 6, and 7 were selected as input data to

detect hydroxyl-bearing minerals, while bands 2, 4, 5, and 6 were selected as input data to detect iron oxide minerals. The eigenvector loadings calculated for mapping hydroxyl-bearing minerals and iron oxides are shown in Tables 2 and 3, respectively.

Table 2 - Calculated eigenvector loadings of the principal components (PCs) applied to bands 2, 5, 6, and 7 of the Landsat-8 data to locate hydroxyl-bearing minerals in the Muteh district.

Components	Band 2	Band 5	Band 6	Band 7
PC1	-0.1967	-0.50877	-0.61679	-0.56748
PC2	-0.24315	-0.8024	0.421117	0.34596
PC3	0.456861	-0.1731	-0.59235	0.640657
PC4	0.832746	-0.2595	0.302247	-0.3845

As hydroxyl-bearing minerals show a high reflectance feature in band 6 and a high absorption feature in band 7, components with high magnitude eigenvector loadings for band 7, irrespective of their sign, and high loadings of the opposite sign for band 6 can be taken into account for the recognition of the hydroxyl-bearing minerals (Table 2). In the PC3 image, the differences in the eigenvector loadings between the two mentioned bands are the largest and, therefore, by considering the negative loading in band 6 and the positive loading in band 7, the hydroxyl-bearing minerals in this component appear in dark colour. To show the pixels in bright colour, the inversed PC3 image was used to locate hydroxyl-bearing minerals as bright pixels.

Table 3 - Calculated eigenvector loadings of the principal components (PCs) applied to bands 2, 4, 5, and 6 of Landsat-8 data for mapping iron oxide minerals.

Components	Band 2	Band 4	Band 5	Band 6
PC1	0.217753	0.476804	0.564998	0.637196
PC2	0.269116	0.332326	0.479823	-0.7661
PC3	0.523551	0.538315	-0.66038	0.003823
PC4	0.778495	-0.61027	0.12021	0.08403

The high reflectance features of iron oxide minerals in band 4, the absorption features in band 2 of the Landsat-8 data, and also the eigenvector loadings in Table 3, have been taken into consideration and the largest loading differences between these two bands are shown in PC4. The iron oxide minerals have a dark colour in this component due to the negative loadings in band 4. Therefore, the PC4 image is the best component to locate iron oxide minerals as bright pixels. Fig. 7d is the colour composite map of the selected components [RGB: -PC3, (-PC3+PC4)/2, PC4] that enhances the hydrothermal alteration zones and iron oxides in white-yellow and dark blue pixels, respectively.

4.4. Spectral analysis

Spectral analysis of the satellite imagery data is an effective approach to distinguish argillic, phyllic, silica, and propylitic hydrothermal alteration minerals, and iron oxides. By using field

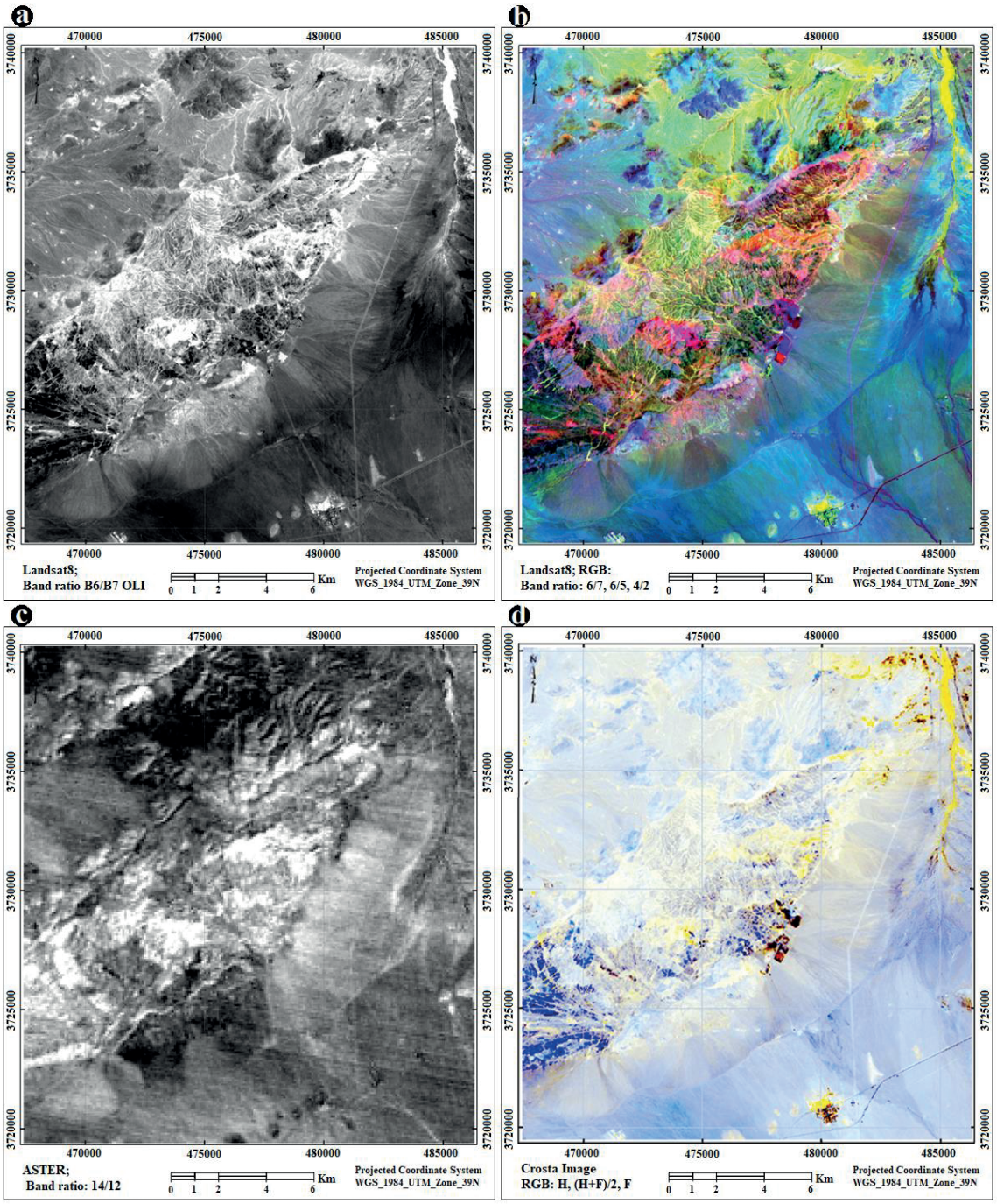

Fig. 7 - a) The 6/7 band ratio image of the Landsat-8 data showing the hydroxyl-bearing clay minerals in bright pixels; b) the colour composite image of three band ratios (R: 6/7, G: 6/5, and B: 4/2) showing the hydrothermal alterations in colours from red to orange; c) the 14/12 band ratio image showing zones of silicification in bright pixels, and d) the colour composite image of the selected PCs [RGB: -PC3, (-PC3+PC4)/2, PC4], showing hydroxyl-bearing minerals from yellow to white-yellow pixels, and the iron oxides in dark blue pixels (modified after Mokhtari *et al*., 2023).

and library spectra, image processing methods such as SAM and MF were applied to the ASTER satellite imagery data of the Muteh district to map these minerals.

4.4.1. Matched filtering (MF)

The MF method is a spectral analysis technique that increases the reflectance of defined reference elements and minimises the reflectance of unknown and undefined composite backgrounds, thus matching the defined character on the image (Harsanyi and Chang, 1994). In other words, it indicates a set of defined reference members in the image by using partial spectral separation. The MF technique first receives the bands on which all corrections have been made, and, then, the spectral reflectance of the minerals is discriminated. Ultimately, the MF method correlates the pure mineral spectrum available in the spectral library with the mineral spectrum from the study area and considers the maximum correlation of the mineral spectrum of the target mineral with the library as a known class. Fig. 8 shows mineral maps of chlorite, kaolinite, muscovite, and silica, identified by the MF technique, as bright pixels, by using library spectra.

4.4.2. Spectral Angle Mapper (SAM)

The SAM method is an effective technique for classifying satellite data based on the comparison of the spectral angles between the library, or field-reference spectra, and the image spectra. The SAM algorithm calculates the spectral similarity by measuring the angle between the two spectra that are considered vectors in an *n*-dimensional space. A wide angle between the two spectra represents low similarity and a narrow angle represents high similarity. The main advantage of this method for satellite data classification is the simplicity and speed of classification based on spectral similarity of feature spectrum and reference spectrum. The SAM method was applied to the ASTER imagery data of the study area to distinguish various alteration minerals. Fig. 9 shows the index map of chlorite, kaolinite, muscovite, and silica minerals, identified by the SAM method, by using library spectra.

4.5. Structural features

Surface structural features related to hydrothermal alteration and outcropping mineralisation could be traced back to their origin in subsurface structures (Brockman *et al*., 1977). The objective of the structural study is to determine the discontinuities in the Earth's crust. These discontinuities, either primary (bedding) or secondary (faults, lineaments, cracks, fractures, and shear zones), could conduct the migration of hydrothermal fluids to create hydrothermal alterations and possible subsequent mineralisation. Both leaner and ring structures can be related to zones of hydrothermal alteration, and ore deposits often form at the intersections of alteration and structures (Mirzababaei *et al*., 2016). Lineaments in satellite imagery data can be detected by applying various image processing methods such as colour composite, band ratio, PCA, filtering, and automated techniques. In this research, various colour combination images of the Sentinel-2A satellite imagery data were used to enhance the lineaments of the Muteh district. These lineaments trend mainly in the NE-SW and NW-SW directions. Most of the known gold deposits/occurrences of the Muteh district are located at the intersections of these two lineaments (Fig. 10).

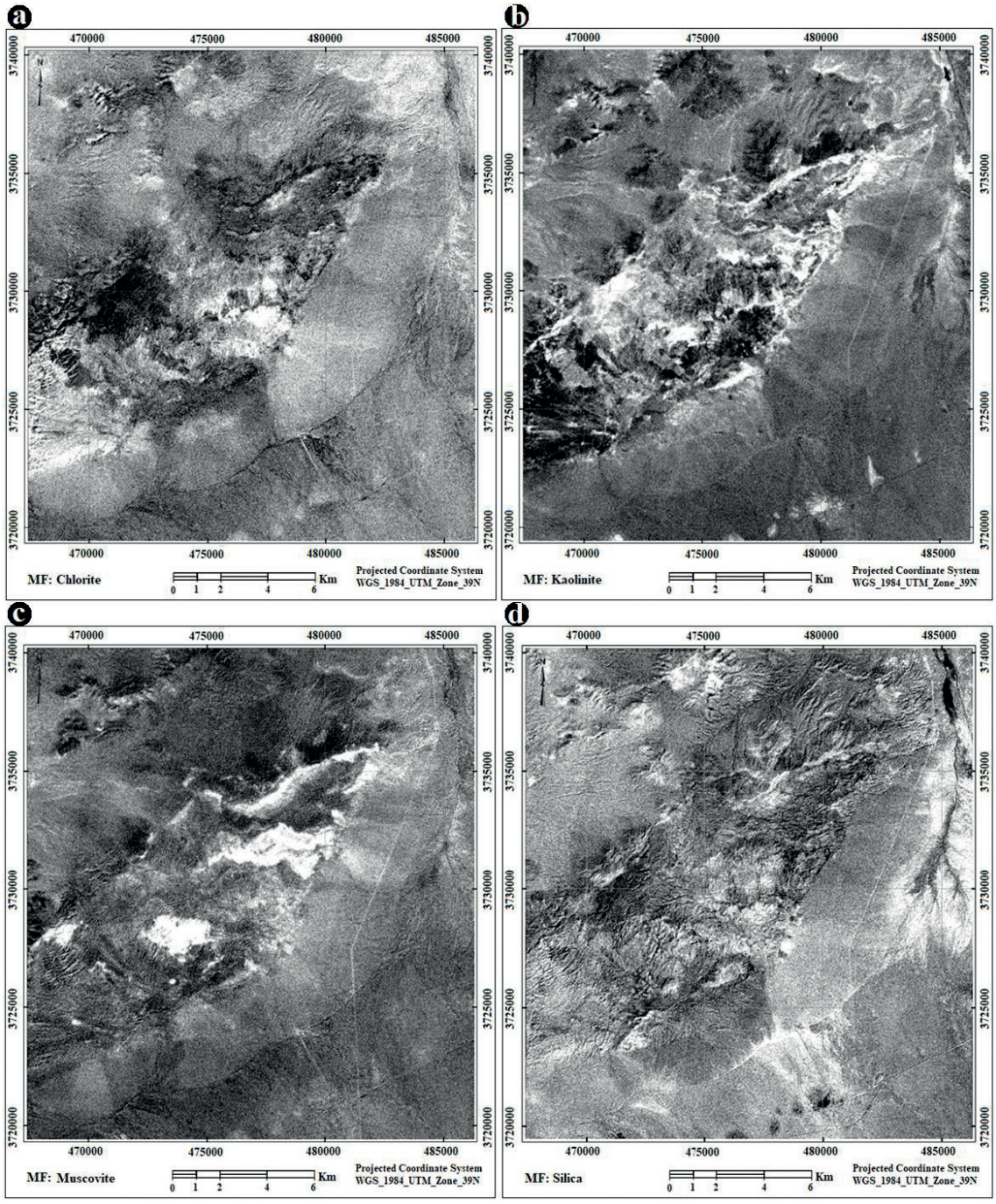

Fig. 8 - By using library spectra, the MF method was applied to the ASTER satellite data of the Muteh district and located: a) chlorite, b) kaolinite, c) muscovite, and d) silica minerals as bright pixels (modified after Mokhtari *et al*., 2023).

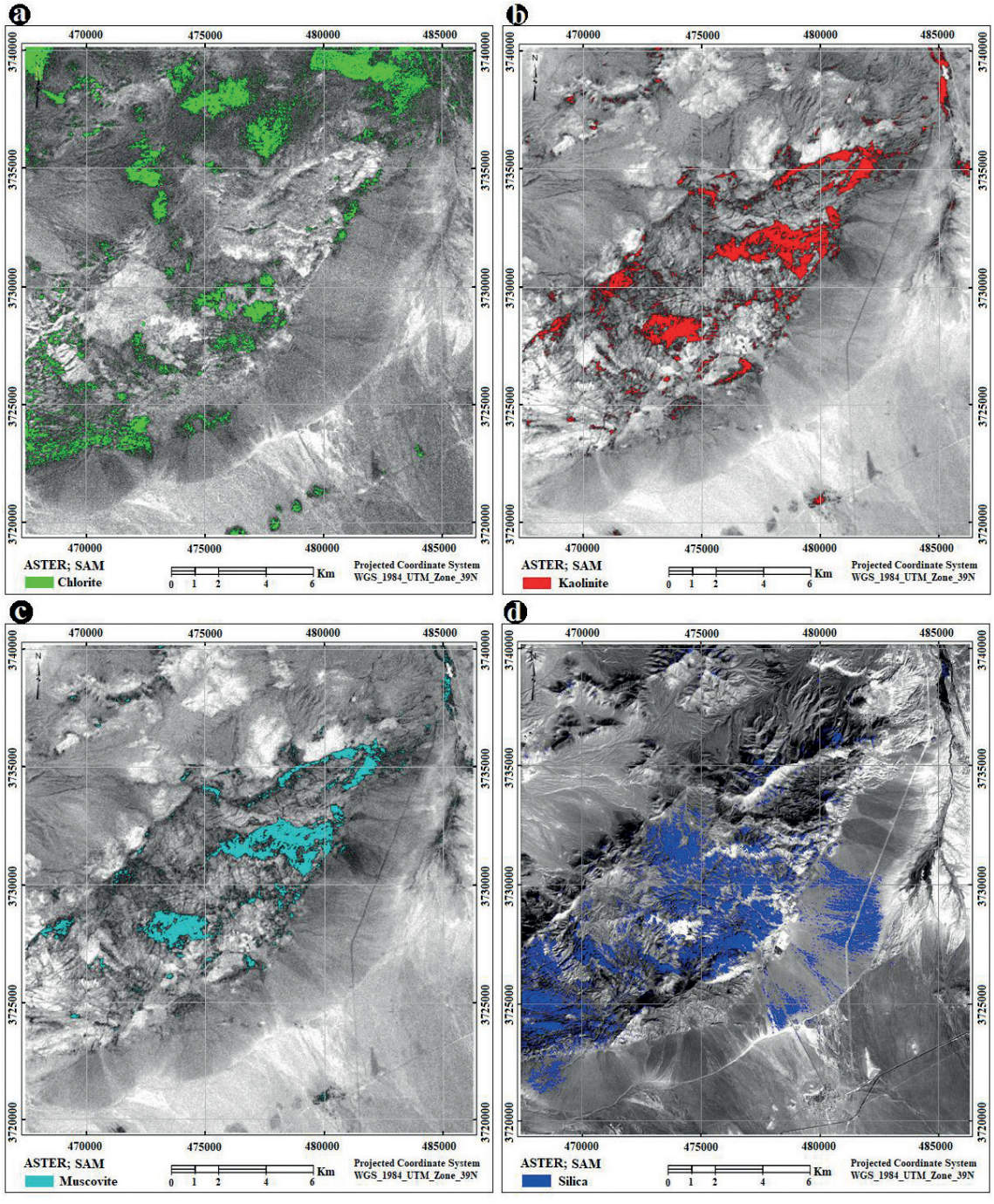

Fig. 9 - By using library spectra, the SAM method was applied to the ASTER satellite imagery data of the Muteh district and located: a) chlorite, b) kaolinite, c) muscovite, and d) silica minerals (modified after Mokhtari *et al*., 2023).

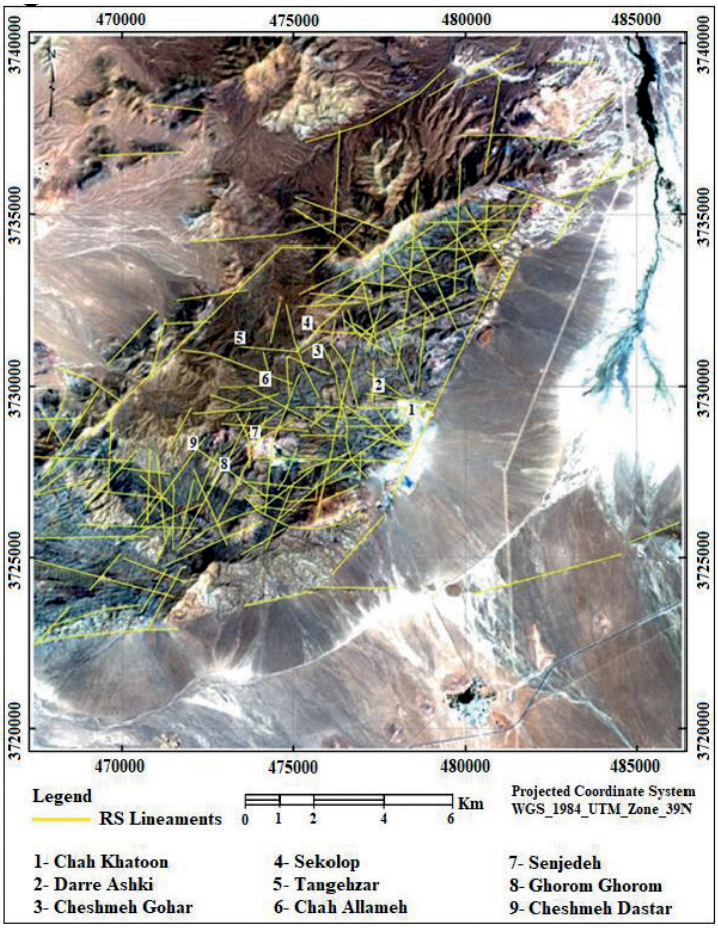

Fig. 10 - Lineament distribution map of the Muteh district, extracted from various colour composite images of the Sentinel-2A satellite imagery data.

4.6. Mapping alteration minerals by using field spectra

In total, 83 measurements were obtained from the 24 samples, collected from the central part of the Muteh district, by using a TerraSpec spectrometer. Some of the prominent sample locations and minerals identified by these measurements are shown in Fig. 18a and Table 4, respectively. The measurements were performed with 3-nm accuracy in the wavelength range from 350 to 2500 nm. After applying the required corrections in the laboratory, the measured spectra were first converted to the ASCII format, followed by various calculations performed on these spectra, and, finally, the measured spectra were converted to the ENVI spectral library format to be used in processing the ASTER data. In the following sections, the index mineral spectra of various hydrothermal alterations, identified by the TerraSpec spectrometer, are compared with similar spectra from the USGS spectral library. Both spectra are, then, used to map and compare the hydrothermal alteration minerals of the study area by processing the ASTER data.

4.6.1. Mapping kaolinite and montmorillonite minerals

Kaolinite $Al_2Si_2O_5(OH)_4$ is the main indicator mineral of argillic alteration which shows strong absorption features in bands 5 and 6 and strong reflection in band 4 of the ASTER data (Hunt and Ashley, 1979; Spatz and Wilson, 1995; Ahmadi *et al.*, 2022). Components such as Al-OH,

Table 4 - Examples of favourable indicator minerals identified by the TerraSpec spectrometer and used in the spectral analysis of the ASTER data.

Sample Number	X-UTM	Y-UTM	Measurement number	Mineral 1	Mineral 2	Mineral 3	Description
Muteh-01	478453	3729162	M-1-CH	Kaolinite	Gypsum		White clay mineral, argillic alteration
Muteh-02	478399	3729074	M-2-CH	Kaolinite	Gypsum	Hematite	Chah Khaton ore, oxidised sulphide
Muteh-06	473542	3727923	M-6-S	Goethite	Smectite	Illite	Creamy clay mineral with iron oxide
Muteh-07	474190	3722787	M-7-S	Chlorite	Silica	Goethite	Silicified propylitic alteration
Muteh-09	474246	3728370	M-9-S	Phengite	Hematite	Illite	Flaky white muscovite, phyllic alteration
Muteh-10	474542	3727721	M-10-S	Phengite	Montmori-ilonite		Senjedeh ore, greenish-grey, foliated surface
Muteh-12	474538	3727976	M-12-S	Phengite	Illite	Goethite	Senjedeh ore, phyllic alteration
Muteh-13	474236	3722789	M-13-S	Hematite	Chlorite		Mostly iron oxide
Muteh-14	473910	3727993	M-14-S	Kaolinite	Phengite	Hematite	Argillic-phyllic alteration
Muteh-18	474276	3728337	M-18-S	Phengite	Chlorite	Kaolinite	White green mineral
Muteh-19	473821	3728325	M-19-S	Phengite	Hematite		Senjedeh ore, phyllic alteration
Muteh-24	473938	3728946	M-24-S	Silica	Phengite	Hematite	Senjedeh ore, silica vein

H_2O, and OH in kaolinite create absorption features (Hunt and Salisbury, 1970). Montmorillonite $(Na,Ca)_{0.3}(Al,Mg)_2Si_4O_{10}(OH)_2 \cdot nH_2O$ shows strong absorption features (minimum reflectance) at 1.4 and 1.9 µm (Hunt and Salisbury, 1970). The absorption and reflectance features in montmorillonite are related to Na, Fe, OH, H_2O, Mg, and Al components. Fig. 11 shows the field spectra of the kaolinite and montmorillonite measured by the TerraSpec spectrometer and the

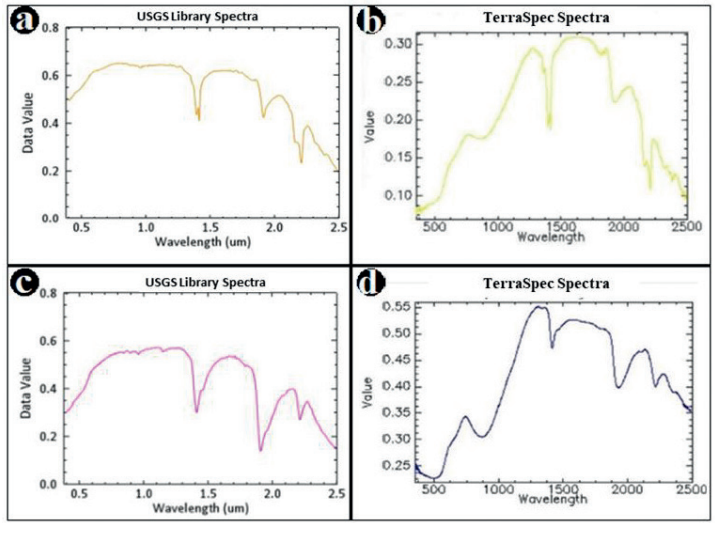

Fig. 11 - Comparison between the mineral spectra resulting from the TerraSpec measurements of the field samples and the corresponding spectra in the USGS spectral library: a) kaolinite library spectrum, b) kaolinite field-referenced spectrum, c) montmorillonite library spectrum, and d) montmorillonite field-referenced spectrum.

corresponding spectra present in the USGS spectral library. The TerraSpec spectra were used to map kaolinite and montmorillonite minerals from the ASTER data of the study area by using the SAM image processing method (Fig. 12).

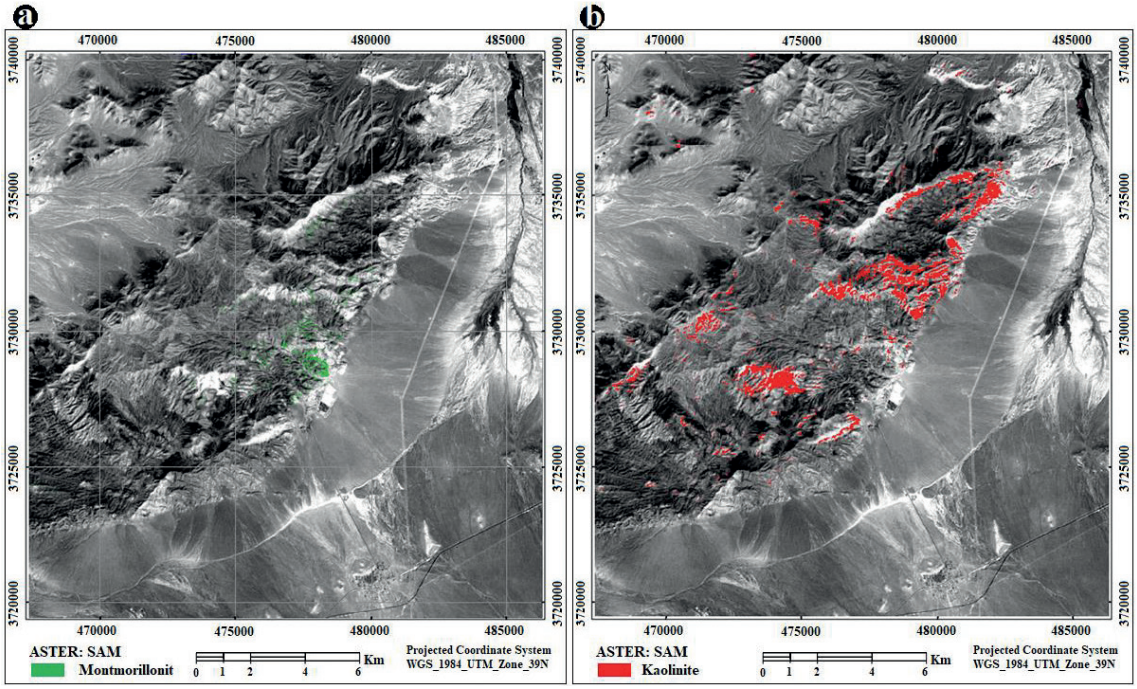

Fig. 12 - Enhancement of ASTER data with the SAM method using the field-referenced spectra obtained from the TerraSpec spectrometer in locating: a) montmorillonite and b) kaolinite minerals in the Muteh district.

4.6.2. Mapping illite and phengite

Phengite $K(AlMg)_2(OH)_2(SiAl)_4$, which is a white fine-grained muscovite mineral, and illite $(KH_3O)(AlMgFe)_2(SiAl)_4O_{10}[(OH)_2(H_2O)]$ are both the main indicator minerals of phyllic alterations that show strong absorption features in bands 8 and 6 and strong reflections in bands 7 and 4 of the ASTER data (Abrams *et al.*, 1983). Fig. 13 shows the field spectra of illite and phengite minerals measured by the TerraSpec spectrometer and also the corresponding spectra present in the USGS spectral library. The TerraSpec spectra were used to map illite and phengite minerals from the ASTER data by using the SAM method (Fig. 14).

4.6.3. Chlorite

Chlorite $(Mg,Fe,Mn,Al)_{12}$ $[(Si,Al)_8O_{20}](OH)_{16}$ is the main indicator of propylitic alteration minerals that shows strong absorption features in band 8 and strong reflections in bands 9 and 4 (Rowan *et al.*, 2003). The components such as H_2O, Fe-OH, and Mg cause absorption and reflection features in chlorite. Figs. 15a and 15b show a comparison between the chlorite field-referenced spectrum obtained from the TerraSpec spectrometer and the corresponding spectra in the USGS spectral library. The TerraSpec spectra were used to map the chlorite in the ASTER data of the study area by using the SAM method (Fig. 16a).

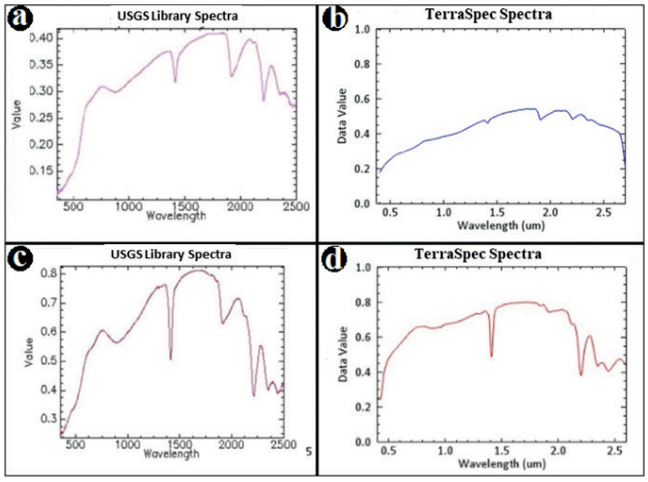

Fig. 13 - Comparison between the field sample spectra measured by the TerraSpec spectrometer and the similar spectra in the USGS spectral library: a) illite library spectrum, b) illite field-referenced spectrum, c) muscovite library spectrum, and d) phengite field-referenced spectrum.

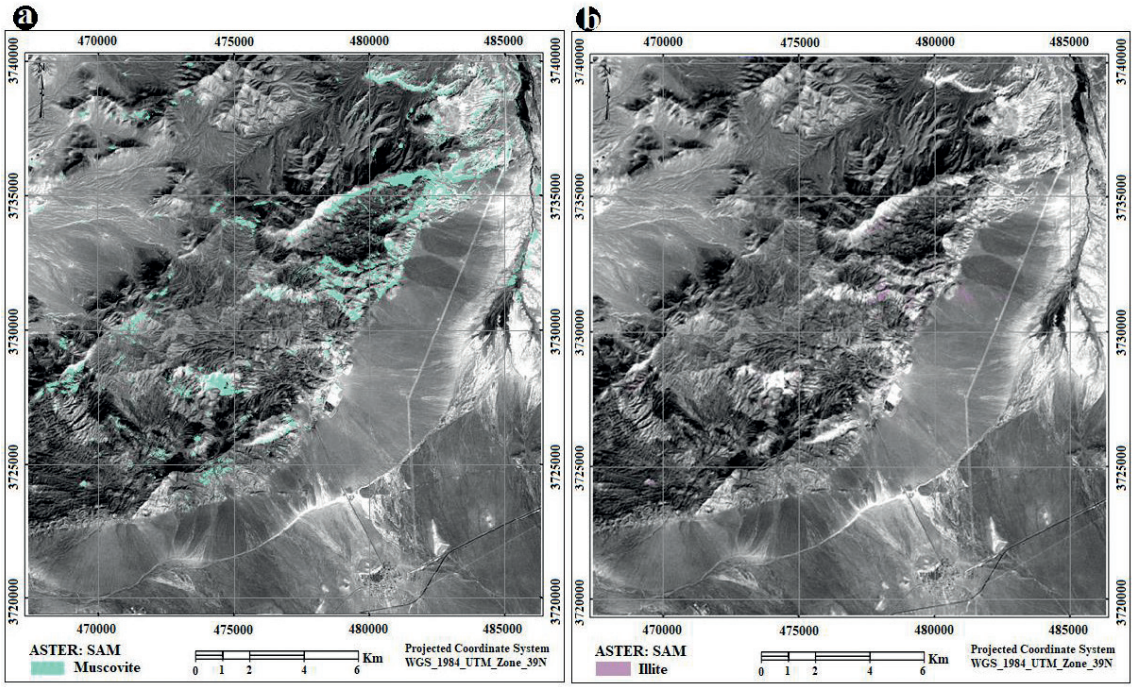

Fig. 14 - Enhancement of the ASTER data with the SAM method using the field-referenced spectra obtained from the TerraSpec spectrometer in locating: a) phengite and b) illite minerals in the Muteh district.

4.6.4. Silicification

Silica (SiO_2) is the main component of silicification that often occurs in a variety of ways in terms of shape and intensity, including massive silica veins and silica caps. Figs. 15c and 15d show the comparison between the field-referenced silica spectrum obtained from the TerraSpec spectrometer and the corresponding spectrum in the USGS spectral library. The silica field-referenced spectra were used to map zones of silicification by using the SAM method (Fig. 16b).

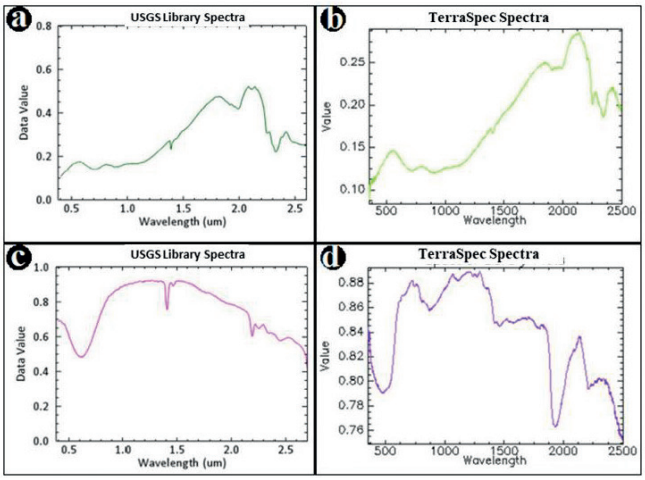

Fig. 15 - Comparison between the field-referenced mineral spectra measured by the TerraSpec spectrometer and the corresponding spectra present in the USGS spectral library: a) chlorite library spectrum, b) field-referenced chlorite spectrum, c) silica library spectrum, and d) field-referenced silica spectrum.

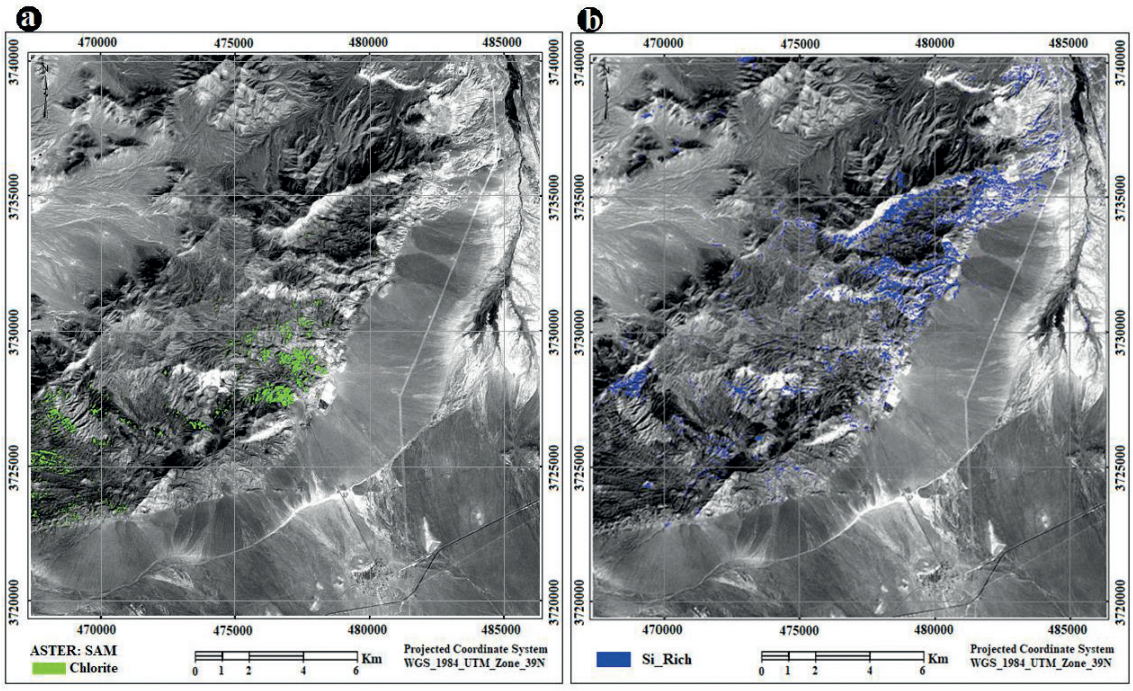

Fig. 16 - Enhancement of the ASTER data with the SAM method using the field-referenced spectra obtained from the TerraSpec spectrometer to locate: a) chlorite and b) silica minerals in the Muteh district.

4.7. Mapping iron oxides

Hematite Fe_2O_3 and goethite FeO(OH) are the main iron oxide minerals associated with gold mineralisation in the Muteh district. Due to the oxidation of sulphide minerals such as pyrite and chalcopyrite, these minerals are often associated with hydrothermal alterations, where there could be evidence of metallic mineralisation. The iron oxides were identified by applying the SAM method to the ASTER imagery data using the TerraSpec field spectra (Fig. 17).

5. Discussion and target selection

Mapping hydrothermal alteration minerals and iron oxides is significant in regional mineral exploration. Phyllic (illite, white micas including sericite, muscovite or phengite), argillic (kaolinite), propylitic (chlorite), and silica alterations, accompanied by iron oxides, are important features associated with various types of mineral deposits. In this research, by using the USGS library spectra, various image processing methods were initially applied to the ASTER, Sentinel-2A, and Landsat-8 satellite imagery data of the Muteh gold mining district, and several minerals in various zones of hydrothermal alteration were identified. Some of these minerals could be associated with gold mineralisation of the orogenic type. After performing post-processing steps, such as thresh-holding and conversion to vector format, all the identified minerals were combined in a single mineral index map (Fig. 18b). The minerals, indicative of various hydrothermal alterations and iron oxides in the mineral index map, were used to create a combined potential target map (Fig. 18a).

In addition, field-referenced spectra of the most favourable indicator minerals associated with the orogenic gold mineralisation of the area, such as phengite, kaolinite, illite, chlorite, and hematite, identified by the TerraSpec spectrometer (Table 4), were also used to process ASTER satellite imagery data of the Muteh district. The location of the important samples that were analysed by the TerraSpec spectrometer is shown in Fig. 19a. Phengite is a key indicator mineral associated with Senjedeh, the largest and most important active gold mine in the district. This mineral was not considered in processing the ASTER data by using library spectra. Based on the presence of phengite and other important alteration minerals, among which illite, kaolinite, chlorite, and hematite, and considering the structural controls (Fig. 10) and known mineral

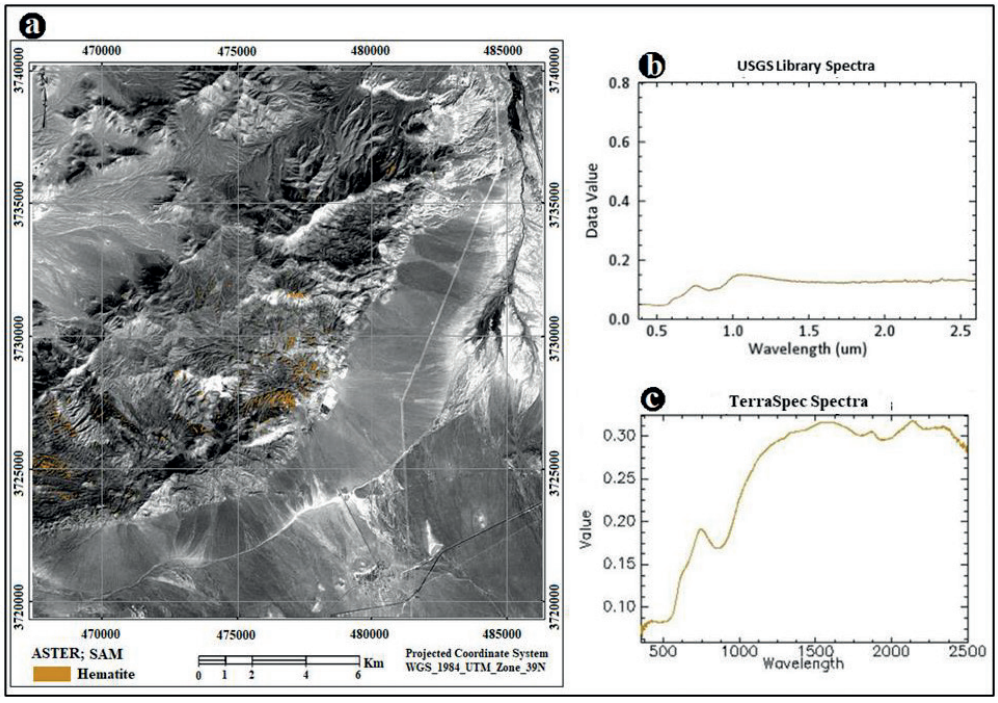

Fig. 17 - a) Enhancement of the ASTER data by the SAM method using the field-referenced spectra obtained from the TerraSpec spectrometer, b) hematite spectrum of the USGS spectral library, and c) hematite field-referenced spectrum obtained by using the TerraSpec spectrometer in the Muteh area.

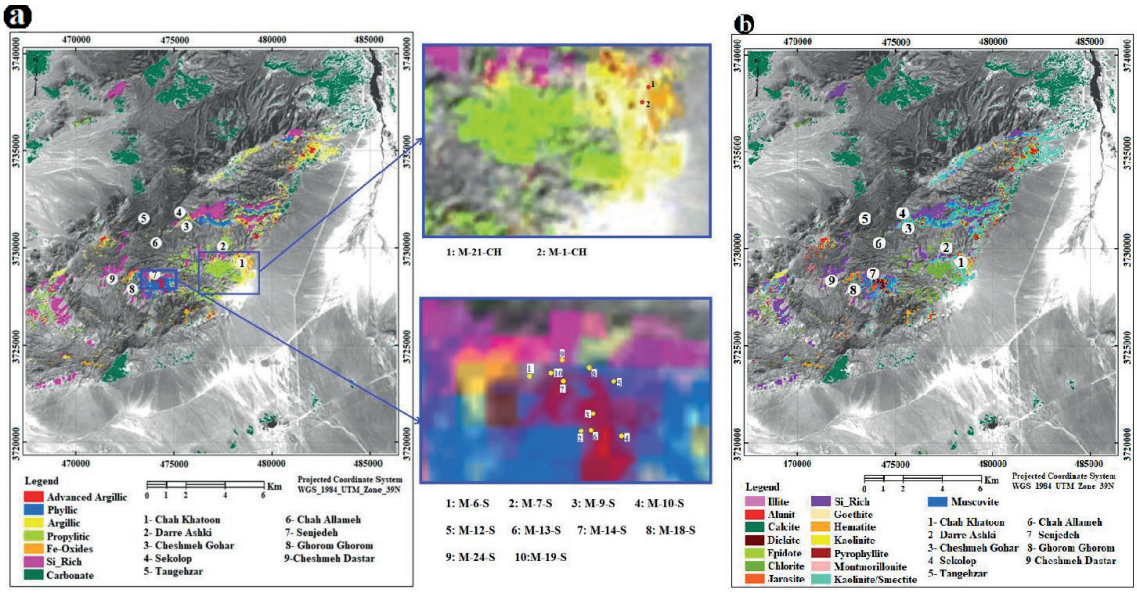

Fig. 18 - Map of various hydrothermal alterations and iron oxides of the Muteh gold mining district, which was created: a) by using the mineral index map of the area and b) by spectral analysis of the ASTER data utilising the USGS library spectra (modified after Mokhtari *et al*., 2023). Map in panel a also shows some of the sample locations in the Senjedeh and Chah Khaton gold deposit areas that were mostly used to measure field-referenced spectra for further processing of the ASTER data.

deposits/occurrences of the study area, four high-potential areas, marked with orange circles, are proposed for future follow-up field exploration (Fig. 19).

6. Validation

The targets mapped by the spectral analysis of the ASTER satellite data were compared with the known gold deposits of the Muteh gold mining district during image processing for confirmation. In addition, for further validation of these targets, field observation and sampling of the mapped high-potential areas were carried out and 11 samples were collected for chemical analysis. These samples were analysed by the XRD method to confirm the hydrothermal alteration minerals identified by the TerraSpec spectrometer and were mapped by processing the ASTER data. Minerals such as quartz (silica), kaolinite, illite, chlorite, muscovite, alunite, albite, dolomite, and hematite were identified by XRD analyses (Table 5). The XRD results confirmed most of the similar minerals identified by the TerraSpec spectrometer and mapped by ASTER data using the SAM method. Phengite, montmorillonite, and smectite were the only minerals that were not identified by the XRD analysis. The XRD results also showed a better correlation with the hydrothermal alteration minerals identified from the ASTER satellite imagery data using field-referenced spectra, compared with the library spectra.

Four samples were also analysed for gold and related elements by using ICP-MS and AAS methods. High gold, copper, arsenic, lead, zinc, and sulphur concentrations were identified in three samples (Table 6). The samples that contained high concentrations of gold and associated elements were mostly correlated with the phengite mineral in the phyllic alteration and silicification zones that mostly contained high hematite and sulphide minerals.

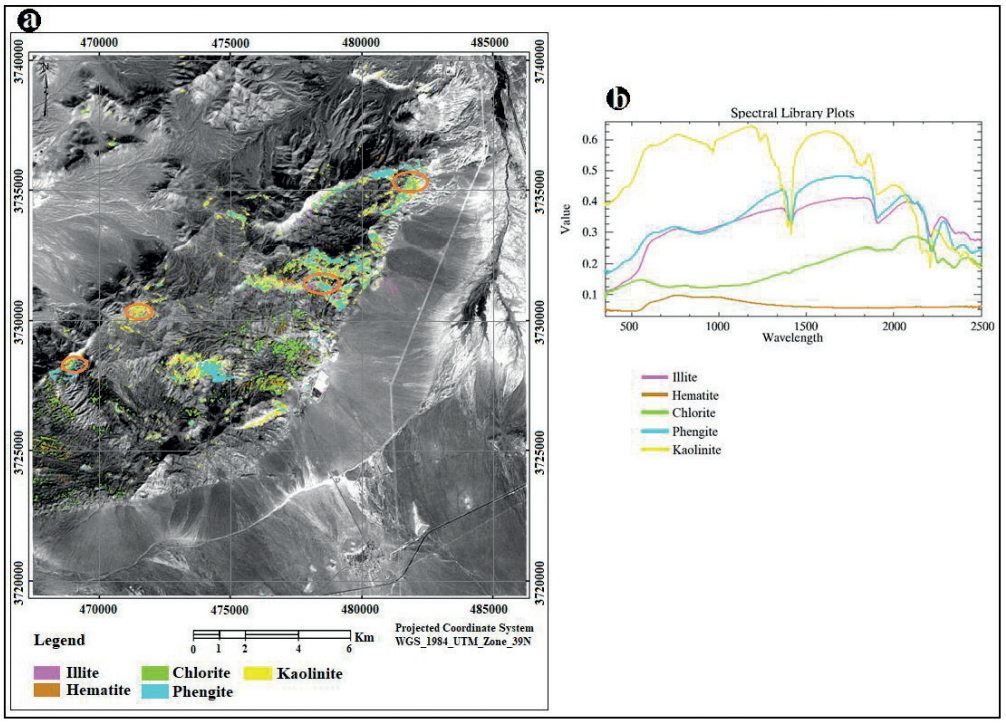

Fig. 19 - a) Integrated map of phengite, illite, kaolinite, chlorite, and hematite indicator minerals, associated with hydrothermal alterations and possible gold mineralisation in the Muteh mining district. The map was generated by using field-referenced spectra in processing the ASTER satellite data with the SAM method, four high-potential areas for future exploration are indicated with orange circles; b) field-referenced spectra of the indicator minerals measured by spectrometry of the field samples using the TerraSpec spectrometer.

7. Conclusions and recommendations

In the Muteh mining district, three sets of satellite imagery data, with different resolutions, were processed and interpreted by utilising both field-referenced and library spectra to map hydrothermal alteration minerals and lineaments for gold exploration. The concluding results of this research are as follows:

- minerals such as illite, muscovite, and phengite in phyllic alteration, kaolinite in argillic alteration, chlorite in propylitic alteration, and quartz in silicification, as well as hematite and goethite oxidised from sulphide minerals, are important indicator minerals in the orogenic gold deposit at the Muteh gold mining district, which can be identified by spectral analyses of appropriate satellite imagery data;
- various methods, such as false colour composite, band ratio, PCA, SAM, and MF, were employed to use reference spectra from the USGS library or field-referenced spectra at the Muteh district to map various minerals associated with hydrothermal alterations by using ASTER, Sentinel-2A, and Landsat-8 satellite imagery data. Based on the field information of the mapped targets for gold exploration, the SAM image processing method provided more accurate results in processing the ASTER data;
- mineral spectra, acquired from the field samples by using the TerraSpec instrument, provided more accurate results in mapping indicator hydrothermal alteration minerals associated with gold mineralisation by processing ASTER satellite data, compared to the

Table 5 - The XRD analyses of the field samples used for validation.

Trace phase	Minor phase	Major phase	UTM		Sample no.
			Y	X	
-	Muscovite, illite, chlorite, pyrite	Quartz, potassium feldspar	3729209	478647	M-1-CH
Pyrite, chlorite	Albite, potassium feldspar, muscovite, illite	Quartz	3728437	474009	M-6-S
Quartz	Kaolinite, muscovite, illite	Alunite	3728200	474244	M-7-S
-	Albite, pyrite	Quartz, muscovite, illite, potassium feldspar	3728282	474298	M-9-S
Hematite	Potassium feldspar, chlorite	Quartz, albite, mica, illite	3728173	474449	M-10-S
-	Potassium feldspar, pyrite	Quartz, albite, muscovite, illite	3728434	474416	M-12-S
-	Potassium feldspar, albite, goethite, kaolinite	Quartz, muscovite, illite	3728202	474291	M-13-S
-	Potassium feldspar, kaolinite	Quartz, albite, muscovite, illite	3728420	474162	M-14-S
Hematite, calcite	Potassium feldspar, vermiculite	Quartz, albite, chlorite, mica, illite	3728484	474289	M-18-S
-	-	Dolomite	3729383	478712	M-21-CH
-	Calcite	Quartz, dolomite	3728517	474162	M-24-S

Table 6 - The ICP-MS and AAS analytical results of gold and other elements.

Element	Unit	Clarke value	Sample no.			
			X:474291	X:474103	X:478712	X:474162
			Y:3728202	Y:3728458	Y:3729383	Y:3728517
			M-13 s	M-19 ch	M-21 ch	M-24 s
Au	ppb	5	250.49	28	4	13
Ag	ppm	0.1	5.6	0.1	0.1	0.2
As	ppm	1.8	224	46	475	51
Cd	ppm	0.2	11.9	2.1	1.0	1.7
Cu	ppm	55	9.795%	1822	111	48
Mo	ppm	1.5	676	18	2	1
Pb	ppm	13	1817	362	133	109
S	%	0.026	0.19	0.24	0.06	0.09
Sb	ppm	0.2	5	4	5	4
Sr	ppm	375	137	50	102	32
Ti	%	0.44	0.04	0.06	0.01	0.01
Zn	ppm	70	696	111	2553	191

corresponding spectra selected from the USGS spectral library used in mapping similar alteration minerals;

- phengite mineral, which was identified by using the TerraSpec spectrometer in this research, is an important indicator mineral associated with gold mineralisation in the Muteh gold mining district. The spectral characteristic of this mineral can be used in satellite image processing of similar geologic settings of orogenic gold mineralisation systems, elsewhere;

- field observation and geochemical analyses in some of the collected field samples confirmed the presence of some of the high-potential areas for gold exploration proposed by processing satellite imagery data. Based on the final combined mineral maps generated by processing the ASTER data using field-referenced spectra, four important target areas are proposed for future follow-up exploration in the Muteh gold mining district.

Acknowledgments. The authors would like to thank the mining company Dorsa Pardazeh for providing the spectrometry results of the specimens of the study area and for its cooperation during the research. We are also grateful to the Geosense Dutch company for measuring and providing the spectral analyses of the field samples.

REFERENCES

Abrams M.J., Brown D., Lepley L. and Sadowski R.; 1983: *Remote sensing for porphyry copper deposits in southern Arizona.* Econ. Geol., 78, 591-604, doi: 10.2113/gsecongeo.78.4.591.

Ahmadi F., Aghajani H. and Abedi M.; 2022: *Mineral potential mapping using satellite images of Sentinel-2, Landsat-8 and ASTER for Iron Ore at Esfordi 1:100000 Sheet.* J. Miner. Resour. Eng., 7, 1-23, doi: 10.30479/JMRE.2021.14427.1458.

Akbari Z., Rasa A., Adabi M.H. and Mohajel M.; 2015: *Mapping of rock units in Ahangaran region (southeast of Malayer) based on ASTER data.* J. Earth Sci. Res., 6, 57-38, (in Persian), <sid.ir/paper/207361/fa>.

Alavipanah S.K.; 2003: *Application of Remote Sensing in Geosciences (Soil Sciences).* The University of Tehran, Tehran, 530 pp., <adinehbook.com/gp/product/9640347884>.

Ali-Bik M.W., Abd El Rahim S.H., Wahab W.A., Abayazeed S.D. and Hassan S.M.; 2017: *Geochemical constraints on the oldest arc rocks of the Arabian-Nubian Shield: the late Mesoproterozoic to late Neoproterozoic Sa'al volcano-sedimentary complex, Sinai, Egypt.* Lithos, 284, 310-326, doi: 10.1016/j.lithos.2017.03.031.

Ali-Bik M.W., Hassan S.M., Abou El Maaty M.A., Abd El Rahim S.H., Abayazeed S.D. and Wahab W.A.; 2018: *The late Neoproterozoic Pan-African low-grade metamorphic ophiolitic and island-arc assemblages at Gebel Zabara area, central eastern Desert, Egypt: petrogenesis and remote sensing-based geologic mapping.* J. Afr. Earth Sci., 144, 17-40, doi: 10.1016/j.jafrearsci.2018.04.001.

Arghavanian A., Darvishzadeh R., Rasa A. and Hosseini Asl A.; 2011: *Extraction of areas with gold potential in the western region of Meshkinshahr using HYPERION images.* J. Remote Sens. and GIS, 3, 91-106, (in Persian).

Asadi Haroni H. and Tabatabai S.H.; 2016: *Mapping hydrothermal alterations in the Muteh gold mining area in Iran by using ASTER satellite imagery data.* EGU General Assembly, Vienna, Austria, <https://ui.adsabs.harvard.edu/abs/2016EGUGA..18.9519A/abstract>.

Asran A.M. and Hassan S.M.; 2019: *Remote sensing-based geological mapping and petrogenesis of Wadi Khuda Precambrian rocks south eastern desert of Egypt with emphasis on leucogranite.* Egypt. J. Remote Sens. Space Sci., 24, 15-27, doi: 10.1016/j.ejrs.2019.07.004.

Bennett S.A., Atkinson W.W. and Kruse F.A.; 1993: *Use of thematic mapper imagery to identify mineralization in the Santa Teresa district, Sonora, Mexico.* Int. Geol. Rev., 35, 1009-1029, doi: 10.1080/00206819309465572.

Brockmann C.E., Fernandez A., Ballon R. and Claure H.; 1977: *Analysis of geological structures based on Landsat-1 images*. In: Remote Sensing Applications for Mineral Exploration, Dowden, Hutchinson and Ross Inc., Stroudsburg, PA, USA, pp. 292-317.

Chang Z. and Yang Z.; 2012: *Evaluation of inter-instrument variations among short wavelength infrared (SWIR) devices.* Econ. Geol., 7, 1479-1488, doi: 10.2113/econgeo.107.7.1479.

Crosta A.P. and Moore J.M.; 1989: *Enhancement of Landsat thematic mapper imagery for residual soil mapping in SW Minas Gerais State Brazil, a prospecting case history in greenstone belt terrain.* In: Proc. 7th ERIM Thematic Conference on Remote Sensing for Exploration Geology, Calgary, Canada, pp. 1173-1187, doi: 10.4236/abb.2020.1111032.

Di Tommaso I. and Rubinstein N.; 2007: *Hydrothermal alteration mapping using ASTER data in the Infiernillo porphyry deposit, Argentina.* Ore Geol. Rev., 32, 275-290, doi: 10.1016/j.oregeorev.2006.05.004.

Ducart D.F., Crósta A.P., Filho C.R.S. and Coniglio J.; 2006: *Alteration mineralogy at the Cerro La Mina epithermal prospect, Patagonia, Argentina: field mapping, short-wave infrared spectroscopy, and ASTER images.* Econ. Geol., 101, 981-996, doi: 10.2113/gsecongeo.101.5.981.

Farhangi A.; 1982: *Report on the exploration and equipping of the Muteh Gold Mine, the description of the operations performed from 1980 to 1981.* Iran's General Mines Stock Company, Ministry of Mines, Industry and Trades, 170 pp.

Ferrier G., White K., Griffiths G., Bryant R. and Stefouli M.; 2002: *Mapping of hydrothermal alteration zones on the island of Lesvos, Greece using an integrated remote sensing dataset.* Int. J. Remote Sens., 23, 341-356, doi: 10.1080/01431160010003857.

Gabr S.S., Hassan S.M. and Sadek M.F.; 2015: *Prospecting for new gold-bearing alteration zones at El-Hoteib area, south eastern Desert, Egypt, using remote sensing data analysis.* Ore Geol. Rev., 71, 1-13, doi: 10.1016/j.oregeorev.2015.04.021.

Gad S. and Kusky T.; 2007: *ASTER spectral rationing for lithological mapping in the Arabian-Nubian Shield, the Neoproterozoic Wadi Kid area, Sinai, Egypt.* Gondwana Res., 11, 326-335, doi: 10.1016/j.gr.2006.02.010.

Ghoneim S.M., Yehia M.A., Salem S.M. and Ali H.F.; 2022: *Integrating remote sensing data, GIS analysis and field studies for mapping alteration zones at Wadi Saqia area, central eastern Desert, Egypt.* Egypt. J. Remote Sens. Space Sci., 25, 323-336, doi: 10.1016/j.ejrs.2022.02.001.

Gupta R.P.; 1991: *Remote Sensing Geology*. Springer-Verlag, Berlin, Germany, 356 pp., <link.springer.com/book/10.1007/978-3-662-05283-9>.

Harsanyi J.C. and Chang C.I.; 1994: *Hyperspectral image classification and dimensionality reduction: an orthogonal subspace projection approach.* IEEE Trans. Geosci. Remote Sens., 32, 779-785, doi: 10.1109/36.298007.

Hassan S.M. and Ramadan T.M; 2015: *Mapping of the late Neoproterozoic Basement rocks and detection of the gold-bearing alteration zones at Abu Marawat-Semna area, eastern Desert, Egypt using remote sensing data.* Arabian J. Geosci., 8, 4641-4656.

Hassan S.M., Sadek M.F. and Greilin R.O.; 2014: *Spectral analyses of basement rocks in El-Sibai-Umm Shaddad area, central eastern Desert, Egypt, using ASTER thermal infrared data.* Arabian J. Geosci., 8, 6853-6865, doi: 10.1007/s12517-014-1729-8.

Hosseinjani Zadeh M.; 2013: *Evaluating relationship between alteration and mineralization using spectral analysis and processing of multispectral and hyperspectral data, a case study from central part of Dehaj-Sarduiyeh Belt, Kerman Province, SE Iran.* Ph.D. Thesis in Geological Sciences, University of Shiraz, Iran, 127 pp.

Huang J., Chen H., Han J., Deng X., Lu W. and Zhu R.; 2018: *Alteration zonation and short wavelength infrared (SWIR) characteristics of the Honghai VMS Cu-Zn deposit, eastern Tianshan, NW China.* Ore Geol. Rev., 100, 263-279, doi: 10.1016/j.oregeorev.2017.02.037.

Hunt G.R. and Ashley R.P.; 1979: *Spectra of altered rocks in the visible and near infrared.* Econ. Geol., 74, 1613-1629, doi: 10.2113/gsecongeo.74.7.1613.

Hunt G.R and Salisbury J.W.; 1970: *Visible and Near-Infrared Spectra of minerals and rocks - I. Silicate minerals*. Mod. Geol., 1, 283-300.

Immitzer M., Vuolo F. and Atzberger C.; 2016: *First experience with Sentinel-2 data for crop and tree species classifications in central Europe.* Remote Sens., 8, 166, 27 pp., doi: 10.3390/rs8030166.

Irons J.R., Dwyer J.L. and Barsi J.A.; 2012: *The next Landsat satellite: the Landsat data continuity mission.* Remote Sens. Environ., 122, 11-21, doi: 10.1016/j.rse.2011.08.026.

Karimi S., Tabatabaei-Manesh S., Safaei H. and Sharifi M.; 2012: *Metamorphism and deformation of golpayegan metapelitic rocks, Sanandaj-Sirjan zone, Iran.* Petrol., 20, 658-675, doi: 10.1134/S086959111207003X.

Karimpour M.H.; 2005: *Comparison of Qaleh Zari Cu-Au-Ag deposit with other Iron Oxides Cu-Au (IOGC-type) deposits, a new classification.* Iran. J. Crystallogr. Mineral., 24, 340-353, (in Persian).

Lefebvre A., Sannier C. and Corpetti T.; 2016: *Monitoring urban areas with Sentinel-2A data: application to the update of the Copernicus high resolution layer imperviousness degree.* Remote Sens., 8, 606, 21 pp., doi: 10.3390/rs8070606.

Loughlin W.P.; 1991: *Principal component analysis for alteration mapping.* Photogramm. Eng. Remote Sens., 57, 1163-1169.

Mahanta P. and Maiti S.; 2021: *Regional scale alteration mineral mapping using ASTER imagery in sparsely vegetated terrain: a case study from eastern part of South Purulia Shear Zone, India.* International Advanced Research Journal in Science, Engineering and Technology, 8, 597-607.

Mehrabi B., Tale Fazel E. and Shahabifar M.; 2012: *Ore mineralogy and fluid inclusions constraints on genesis of the Muteh gold deposit (western Iran).* Geopersia, 2, 67-90, doi: 10.22059/JGEOPE.2012.24802.

Mirzababaei G., Shahabpour J., Zarasvandi A. and Hayatolgheyb S.M.; 2016: *Structural controls on Cu metallogenesis in the Dehaj area, Kerman porphyry copper belt, Iran: a remote sensing perspective.* J. Sci., Islamic Republic of Iran, 27, 253-267.

Moktari K., Asadi Haroni H., Aliabadi M.A. and Beiranvand S.; 2023: *Identification of hydrothermal alterations in Muteh area, northwest of Isfahan, using satellite images*. Sci. - Res. Quarterly Geog. Data (SEPEHR), 32, 29-47, doi: 10.22131/sepehr.2023.563665.2920.

Moore F., Rastmanesh F., Asadi Haroni H. and Modaberi S.; 2008: *Mineralogical alteration mapping using combined selective principal component analysis and matched filter processing in Takab area, NW Iran.* Int. J. Remote Sens., 10, 2851-2867.

Moritz R., Ghazban F. and Singer B.S.; 2006: *Eocene gold ore formation at Muteh, Sanandaj-Sirjan tectonic zone, western Iran: a result of late-stage extension and exhumation of metamorphic basement rocks within the Zagros Orogen.* Econ. Geol., 101, 1497-1524, doi: 10.2113/gsecongeo.101.8.1497.

Paul F., Winsvold S.H., Kääb A., Nagler T. and Schwaizer G.; 2016: *Glacier remote sensing using Sentinel-2. Part II: mapping glacier extents and surface facies, and comparison to Landsat 8.* Remote Sens., 8, 575, 15 pp., doi: 10.3390/rs8070575.

Pesaresi M., Ehrlich D., Ferri S., Florczyk A., Freire S., Halkia M. and Syrris V.; 2016: *Operating procedure for the production of the Global Human Settlement Layer from Landsat data of the epochs 1975, 1990, 2000, and 2014.* Publications Office of the European Union, Luxembourg, JRC97705, 62 pp., doi: 10.2788/656115.

Rasouli B.M. and Tangestani M.H.; 2020: *A new band ratio approach for discriminating calcite and dolomite by ASTER imagery in arid and semiarid regions.* Nat. Resour. Res., 29, 2949-2965, doi: 10.1007/s11053-020-09648-w.

Rowan L.C., Hook S.J., Abrams M.J. and Mars J.C.; 2003: *Mapping hydrothermally altered rocks at Cuprite, Nevada, using the Advanced Spaceborne Thermal Emission and Reflection Radiometer (ASTER), a new satellite-imaging system.* Econ. Geol., 98, 1019-1027, doi: 10.2113/gsecongeo.98.5.1019.

Ruiz-Armenta J.R. and Prol-Ledesma R.M.; 1998: *Techniques for enhancing the spectral response of hydrothermal alteration minerals in Thematic Mapper images of central Mexico.* Int. J. Remote Sens., 19, 1981-2000, doi: 10.1080/014311698215108.

Sadek M.F.; 2005: *Geology and spectral characterization of the basement rocks at Gabal Gerf area, southeastern Egypt.* In: Proc. SPIE, Ehlers M. and Michel U. (eds), Remote Sensing for Environmental Monitoring, GIS Applications, and Geology V, The International Society for Optical Engineering, Bruges, Belgium, Vol. 5983, pp. 153-163, doi: 10.1117/12.626806.

Sadek M.F., Ramadan T.M., Abu El Leil I. and Salem S.M.; 2006: *Using remote sensing technique in lithological discriminations and detection of gold-bearing alteration zones at Wadi Defiet area, southeastern Desert, Egypt.* In: Proc. SPIE, Ehlers M. and Michel U. (eds), Remote Sensing for Environmental Monitoring, GIS Applications, and Geology VI, The International Society for Optical Engineering, Stockholm, Sweden, Vol. 6366, pp. 104-114, doi: 10.1117/12.685594.

Shokry M.M., Sadek M.F., Osman A.F. and El Kalioubi B.A.; 2021: *Precambrian basement rocks of Wadi-Khuda-Shut area, south eastern Desert of Egypt: geology and remote sensing analysis.* Egypt. J. Remote Sens. Space Sci., 24, 59-75, doi: 10.1016/j.ejrs.2019.12.005.

Spatz D.M. and Wilson R.T.; 1995: *Remote sensing characteristics of porphyry copper systems, western America Cordillera*. In: Pierce F.W. and Bolm J.G. (eds), Porphyry copper deposits of the American Cordillera, Arizona Geological Society Digest, 20, 94-108.

Tangestani M.H. and Moore F.; 2002: *Porphyry copper alteration mapping at the Meiduk area, Iran.* Int. J. Remote Sens., 23, 4815-4825, doi: 10.1080/01431160110115564.

Tavakoli Dehkordi M.A.; 1986: *Detailed exploration of the Muteh gold.* Iran's General Mines Stock Company, Ministry of Mines and Metals, Tehran, Iran, 86 pp. (in Persian).

Van Ruitenbeek F.J., Cudahy T., Hale M. and van der Meer F.D.; 2005: *Tracing fluid pathways in fossil hydrothermal systems with near-infrared spectroscopy.* Geol., 33, 597-600, doi: 10.1130/G21375.1.

Vincent R.K.; 1997: *Fundamentals of geological and environmental remote sensing*. Prentice Hall Series in Geographic Information Science, Upper Saddle River, NJ, USA, 383 pp., doi: 10.1017/S0016756898391505.

Yazdi M., Sadati N., Matkan A. and Ashoorloo D.; 2011: *Application of remote sensing in monitoring of faults.* Int. J. Environ. Res., 5, 457-468, doi: 10.22059/ijer.2011.330.

Yuhas R.H., Goetz A.F. and Boardman J.W.; 1992: *Discrimination among semi-arid landscape endmembers using the spectral angle mapper (SAM) algorithm.* In: Green R.O. (ed), Summaries of the Third Annual JPL Airborne Geoscience Workshop, Pasadena, CA, USA, Vol. 1, pp. 147-149.

Yusefinia N.; 2004: *The study of the fluid inclusions of the Muteh gold ore deposits and the possibility of using it as an exploration criterion to discriminate the gold-bearing and barren zones.* Master Thesis, Faculty of Science, Kharazmi University, Tehran, Iran, 130 pp. (in Persian).

Zerai F.T., Gorsevski P.V., Panter K.S., Farver J. and Tangestani M.H.; 2023: *Integration of ASTER and soil survey data by principal components analysis and one-class support vector machine for mineral prospectivity mapping in Kerkasha, southwestern Eritrea.* Nat. Resour. Res., 32, 2463-2493, doi: 10.1007/s11053-023-10268-3.

Corresponding author: Hooshang Asadi Haroni
Department of Geology, Mahallat Branch, Islamic Azad University
Ayattollah Khomeni boulevard, Mahallat, Iran
Phone: +98 9134028040; e-mail: hooshang@cc.iut.ac.ir